Journal of Materials Chemistry A

COMMUNICATION

View Article Online
View Journal | View Issue

Cite this: J. Mater. Chem. A, 2018, 6, 16308

Received 15th June 2018
Accepted 27th July 2018

DOI: 10.1039/c8ta05706k

rsc.li/materials-a

In situ growth of $(NH_4)_2V_{10}O_{25}\cdot 8H_2O$ urchin-like hierarchical arrays as superior electrodes for all-solid-state supercapacitors†

Yingchang Jiang,[a] Le Jiang,[a] Zeyi Wu,[a] Peiyu Yang,[a] Haitao Zhang,[b] Zhichang Pan[a] and Linfeng Hu *[a]

Hierarchical nanostructures with highly exposed active surfaces for use in high-performance pseudocapacitors have attracted considerable attention. Herein, we developed a one-step method for the *in situ* growth of $(NH_4)_2V_{10}O_{25}\cdot 8H_2O$ urchin-like hierarchical structures on highly conductive nickel foam substrates for use as advanced electrodes for all-solid-state asymmetric supercapacitors. The *in situ* growth of $(NH_4)_2V_{10}O_{25}\cdot 8H_2O$ urchin-like hierarchical structures delivers a specific capacitance of 1530 F g^{-1} at a current density of 1.5 A g^{-1}, and retains 95.1% of the initial capacitance after 10 000 cycles, owing to the advantages of the urchin-like hierarchical structure such as more active sites for electrochemical reactions, as well as a shortened diffusion length for the charge carriers due to a binder-free effect, which exceeds that of most recently reported vanadates and polyvanadates. The as-assembled all-solid-state $(NH_4)_2V_{10}O_{25}\cdot 8H_2O$@Ni//PVA/KOH//RGO@Ni device exhibits a comparable capacity of 92.2 F g^{-1} at a current density of 0.4 A g^{-1} and excellent cycling performance through 5000 cycles. Our study provides rational guidance toward the design of novel hierarchical nanostructures of polyvanadate for solid-state supercapacitors with superior electrochemical performances in long-term cycling stability and high energy density.

Introduction

The rapidly growing use of electronic devices puts forward a new challenge to high-performance devices and technologies for energy storage. Supercapacitors have been receiving considerable attention due to their high power density and fast charging rate.[1] However, the main challenge for the practical application of supercapacitors is their low energy density and unsatisfactory cycling stability.[2] Tremendous effort has been devoted to designing high-capacitance electrode materials for supercapacitors. Recent experimental and theoretical progress on electrochemical energy storage has revealed two emerging strategies for high energy-density supercapacitors: (1) the *in situ* growth of active materials on various conductive current collectors, which has been regarded as an effective route to improving the interfacial contact. Firstly, the as-grown active materials on the current collector without any insulating polymer binder could significantly reduce the "dead volume" and improve the electrochemical activity of the electrode. Secondly, the direct growth of active materials could reduce the interface resistance gap between the substrate and active compounds and act as an electron superhighway to enhance the ion/electron transfer rate.[3–5] (2) The development of novel electrode compounds with electrochemical activity. Recently, vanadates and polyvanadates have been regarded as highly promising electrode materials in energy devices due to the high abundance and mixed oxidation states of vanadium (V^{3+}, V^{4+} and V^{5+}), high theoretical specific capacity and non-toxic characteristics.[6,7] Many previous studies have revealed the advanced electrochemical performance of various vanadium-based compounds, including layered $V_3O_7\cdot H_2O$ fibers,[4] VO_2 nanoparticles,[8] V_2O_3 nanorods,[9] V_2O_5 aerogels,[10] VO_2 nanobelts,[11] graphene & VO_2 nanocomposites,[11] vanadium nitride nanosheets,[12] *etc.*[13–16]

Most recently, polyvanadates, such as MV_3O_8 (M = Li, Na and NH_4), have been reported as a kind of cathode material with high capacity and acceptable structural stability. Typically, Zhou *et al.* synthesized $NH_4V_3O_8\cdot 0.2H_2O$ *via* a soft template assisted method and it exhibited a reversible capacity of 225.9 mA h g^{-1} at a current density of 0.015 A g^{-1} for lithium ion storage.[12] Wang *et al.* reported the electrochemical properties of Ni^{2+} doped $NH_4V_3O_8\cdot 0.2H_2O$ nanoflakes grown *in situ* on Ni foam in a three-electrode cell configuration.[17] However, the study of vanadates as energy storage materials has just started on the leveling line, and the development of novel vanadates for electrochemical device application should be of great interest and highly desired.

[a]Department of Materials Science, Fudan University, Shanghai 200433, P. R. China. E-mail: linfenghu@fudan.edu.cn

[b]Beijing Key Laboratory of Ionic Liquids Clean Process, Institute of Process Engineering, Chinese Academy of Sciences, Beijing 100190, P. R. China

† Electronic supplementary information (ESI) available. See DOI: 10.1039/c8ta05706k

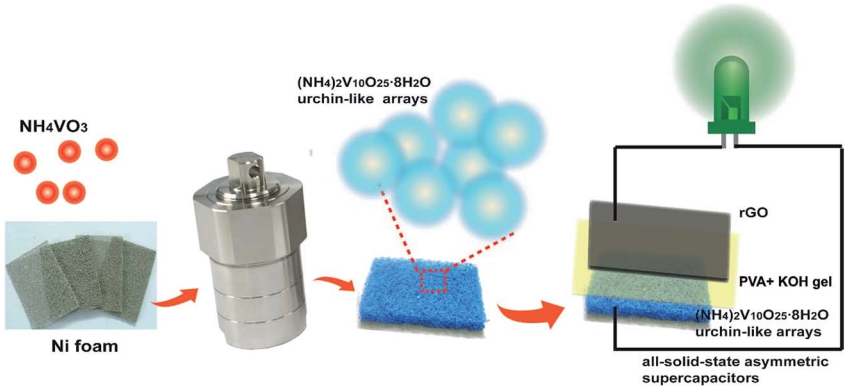

Scheme 1 Schematic illustration of the *in situ* growth of $(NH_4)_2V_{10}O_{25}\cdot 8H_2O$ urchin-like arrays on a Ni foam surface as the electrode of a solid-state supercapacitor.

Three-dimensional (3D) urchin-like hierarchical structures have attracted significant interest owing to their high specific surface area and well-defined morphology. Various urchin-like hierarchical structures have been widely reported for application in solar cells,[18] water treatment,[19] Li-ion batteries[20] and supercapacitors.[21] In this study, we developed a method for the *in situ* growth of $(NH_4)_2V_{10}O_{25}\cdot 8H_2O$ on a Ni foam surface as a high-performance pseudocapacitor electrode (Scheme 1). Interestingly, the as-grown $(NH_4)_2V_{10}O_{25}\cdot 8H_2O$ exhibits urchin-like hierarchical arrays assembled from numerous microwires (length: ~40 μm). This unique hierarchical morphology provides a large surface area and exposed active sites as well as fast ion diffusion. As a result, the $(NH_4)_2V_{10}O_{25}\cdot 8H_2O$ urchin-like hierarchical structure exhibited high specific capacitance (1530 F g^{-1} at 1.5 A g^{-1}) and energy density (53.1 W h kg^{-1} at 375 W kg^{-1}), which exceeds that of most recently reported vanadates and polyvanadates.[10,12,22–26] The as-assembled all-solid-state $(NH_4)_2V_{10}O_{25}\cdot 8H_2O$@Ni//PVA/KOH//RGO@Ni device exhibits a comparable capacity of 92.2 F g^{-1} at a current density of 0.4 A g^{-1} and excellent cycling performance through 5000 cycles. Our study provides rational guidance toward the design of hierarchical nanostructures of vanadates for solid-state supercapacitors with superior electrochemical performances in long-term cycling stability and high energy density.

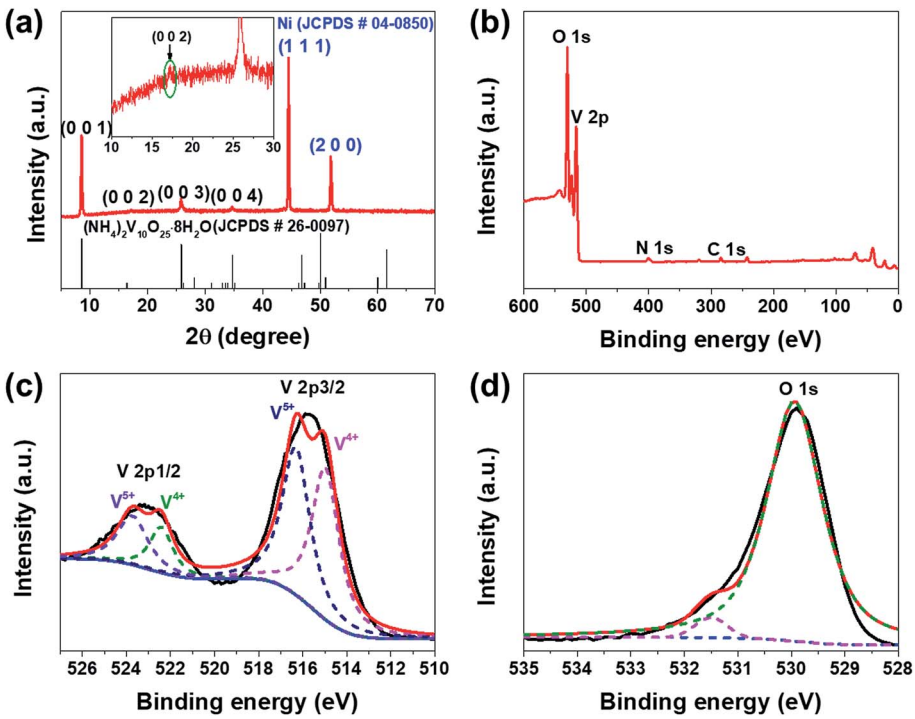

Fig. 1 (a) XRD pattern of the $(NH_4)_2V_{10}O_{25}\cdot 8H_2O$ urchin-like hierarchical structure directly grown on a Ni foam surface. XPS spectra of the $(NH_4)_2V_{10}O_{25}\cdot 8H_2O$ urchin-like hierarchical structure: (b) survey, (c) V 2p, (d) O 1s.

Results and discussion

$(NH_4)_2V_{10}O_{25}\cdot 8H_2O$ urchin-like hierarchical structures were directly grown on nickel foam substrates using a hydrothermal method. As shown in Fig. 1, the phase of the as-grown sample can be indexed into $(NH_4)_2V_{10}O_{25}\cdot 8H_2O$ (JCPDS 26-0097) with $a = 11.54$ Å, $b = 3.64$ Å, $c = 11.12$ Å, $\beta = 112°$, and, $\alpha = \gamma = 90°$. No peaks of impurities were discerned, indicating the high purity of the product. Note that $(00l)$ diffraction of the as-grown $(NH_4)_2V_{10}O_{25}\cdot 8H_2O$ shows much higher intensity compared to other crystal planes (Fig. 1a), suggesting a highly preferred orientation along the $[00l]$ $(l = 0, 1, 2\ldots)$ direction. Moreover, the inset in Fig. 1a shows a weak (002) diffraction peak. X-ray Photoelectron Spectroscopy (XPS) characterization, shown in Fig. 1b–d, was used to examine the chemical states of the elements in the composite. The C 1s, N 1s, O 1s and V 2p regions can be overall observed from the complete survey spectrum of $(NH_4)_2V_{10}O_{25}\cdot 8H_2O$ in Fig. 1b. By using a Gaussian fitting, two obvious shake-up satellites (indicated as "Sat") close to two spin–orbit doublets at 523.4 and 516 eV can be identified as V $2p_{1/2}$ and V $2p_{3/2}$ signals of V^{4+} and V^{5+}, respectively (Fig. 1c). The peak intensity difference in the corresponding peaks suggests the major presence of V^{5+} in the present study. Moreover, the detailed O 1s spectrum, shown in Fig. 1d, shows two major peaks at 529.9 and 531.6 eV. The former corresponds to the lattice oxygen (*i.e.*, O^{2-}), indicating V–O bonding.[27] The latter corresponds to hydroxyl groups, revealing the presence of O–H from the H_2O.[28]

Typical scanning electron microscopy (SEM) images of the as-grown product, shown in Fig. 2a and b, indicate highly dense coverage of a large number of $(NH_4)_2V_{10}O_{25}\cdot 8H_2O$ urchin-like structures on the Ni foam surface. At higher magnification, the SEM images (Fig. 2c and d) show that the urchin-like shape grown perpendicular to the Ni foam surface is assembled from a large amount of microwires with an average length of about 40 μm. These microwires are radially aligned and close-packed, exhibiting a highly developed surface area. The energy dispersive X-ray spectroscopy (EDX) point analysis (Fig. S1†) further confirms the presence of V, O and N elements. During the hydrothermal growth, we found that such an urchin-like structure could just be observed on the Ni foam surface. The powder sediment on the bottom of the hydrothermal autoclave shows quite a different morphology of irregular strips (Fig. S2†). This result suggests that the Ni foam should play an important role in the formation of $(NH_4)_2V_{10}O_{25}\cdot 8H_2O$ urchins, and the *in situ* growth should be induced by heterogeneous nucleation on

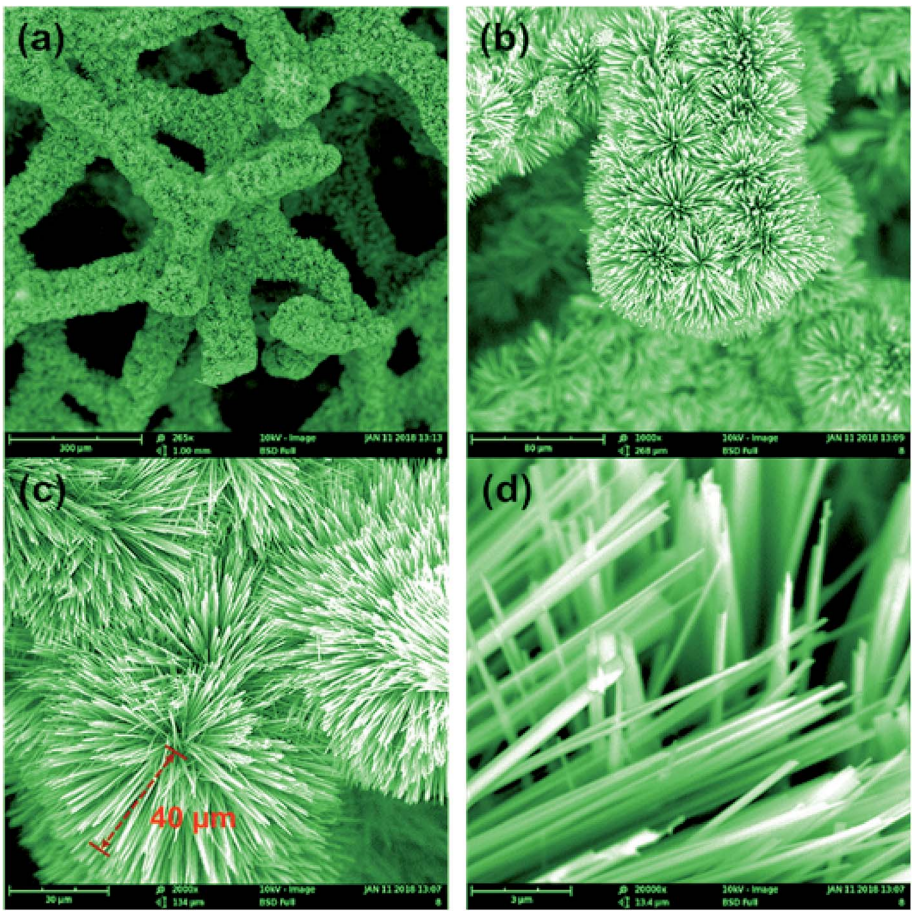

Fig. 2 Typical SEM images of the as-grown hierarchical $(NH_4)_2V_{10}O_{25}\cdot 8H_2O$ urchin-like structures on a Ni foam surface with different magnifications. (a and b) at low magnification; (c and d) at high magnification.

the Ni foam surface. Note that Ni foam was activated by acid to remove the nickel oxide layer on the surface. This treatment is important for the attachment of the $(NH_4)_2V_{10}O_{25}\cdot 8H_2O$ crystal nucleus and the possible growth mechanism of the $(NH_4)_2V_{10}O_{25}\cdot 8H_2O$ urchin may be proposed as follows: during the hydrothermal reaction, NH_4VO_3 converts into $(NH_4)_2V_{10}O_{25}\cdot 8H_2O$ on the surface of Ni foam. The $(NH_4)_2V_{10}O_{25}\cdot 8H_2O$ nuclei gradually grow into the primary particles, which aggregate into chains and partly deposit on the surface of the nickel substrate to form the urchin arrays.

A typical transmission electron microscopy (TEM) image of an individual $(NH_4)_2V_{10}O_{25}\cdot 8H_2O$ microwire is shown in Fig. 3. The layered stacking in this microwire can be clearly distinguished, and the inter-lamellar spacing of the $(NH_4)_2V_{10}O_{25}\cdot 8H_2O$ was around 0.95 nm (Fig. 3b). The as-observed lattice spacing in the HRTEM image was calculated to be 0.35 nm and 0.54 nm, matching well with the (003) plane and (200) plane of monoclinic $(NH_4)_2V_{10}O_{25}\cdot 8H_2O$, respectively. The selected area electron diffraction (SAED) pattern taken from the edge portion of this wire exhibited very sharp diffraction spots (Fig. 3e), demonstrating the single-crystalline nature of each microwire.

The cyclic voltammetry (CV) curve of the as-obtained hybrid composites (Fig. 4a) exhibited reversible redox peaks within the 0.0–0.5 V range, corresponding to the reversible reaction of V(IV) ↔ V(V). This indicates the strong pseudocapacitive nature of the as-obtained electrodes. As shown in Fig. S3,† the overlapping representative CV curves of the $(NH_4)_2V_{10}O_{25}\cdot 8H_2O$ urchin-like hierarchical electrode for the first to hundredth cycles at a scan rate of 20 mV s^{-1} illustrate the steady reversible redox reaction. Fig. 4b shows the galvanostatic charge–discharge curves of the $(NH_4)_2V_{10}O_{25}\cdot 8H_2O$ urchin-like hierarchical@Ni foam hybrid electrode at different current densities. The cycling stability of the material was examined up to 10 000 cycles with ~95.1% capacitance retention at a current density of 8 A g^{-1}, demonstrating its long-term stability and durability (Fig. 4c). Additionally, electrochemical impedance spectroscopy (EIS) was also used to compare the electrochemical properties of $(NH_4)_2V_{10}O_{25}\cdot 8H_2O$@Ni prepared by the *in situ* growth method and a $(NH_4)_2V_{10}O_{25}\cdot 8H_2O$-based electrode with Ni foam as the current collector. Fig. 4d shows the typical Nyquist plots, which consist of a compressed semicircle, a semicircle at a higher frequency region and a spike at lower frequency. At high frequency, the intersection of the curve at the real part indicates the resistance of the electrochemical system (R_s), which includes the inherent resistance of the electroactive material, ionic resistance of the electrolyte and contact resistance at the interface between the electrolyte and the electrode and the

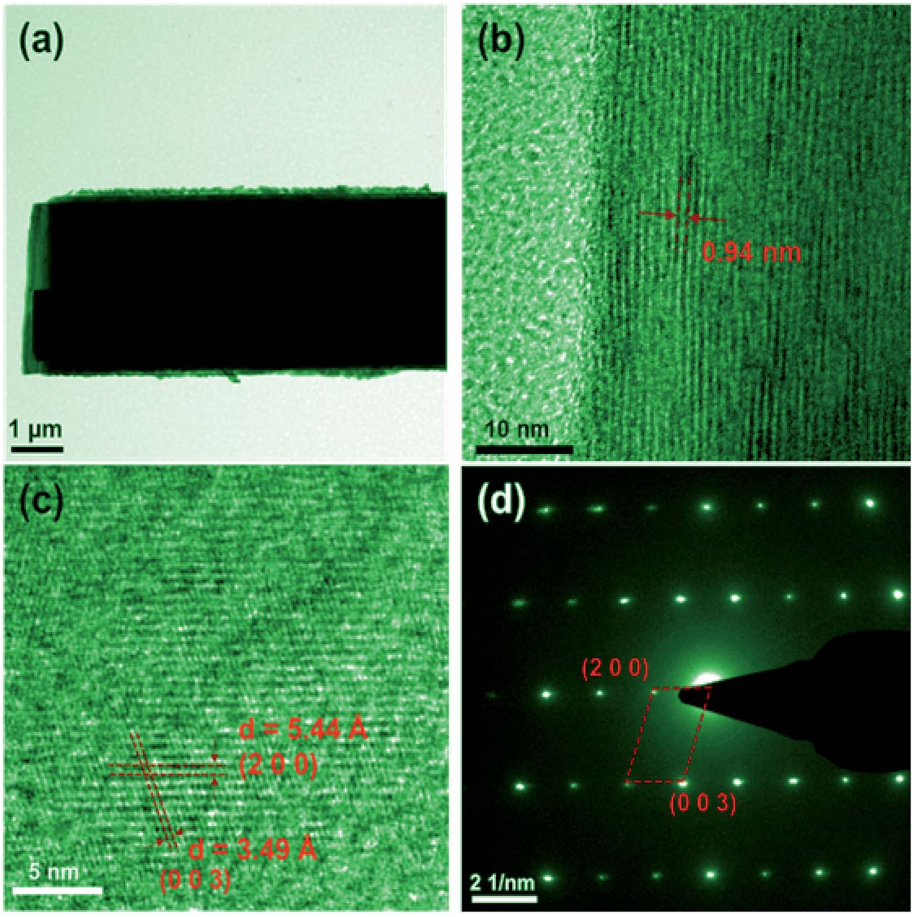

Fig. 3 Typical (a) TEM and (b and c) HRTEM images of an individual $(NH_4)_2V_{10}O_{25}\cdot 8H_2O$ microwire separated from the urchin-like structure. (d) The corresponding SAED pattern.

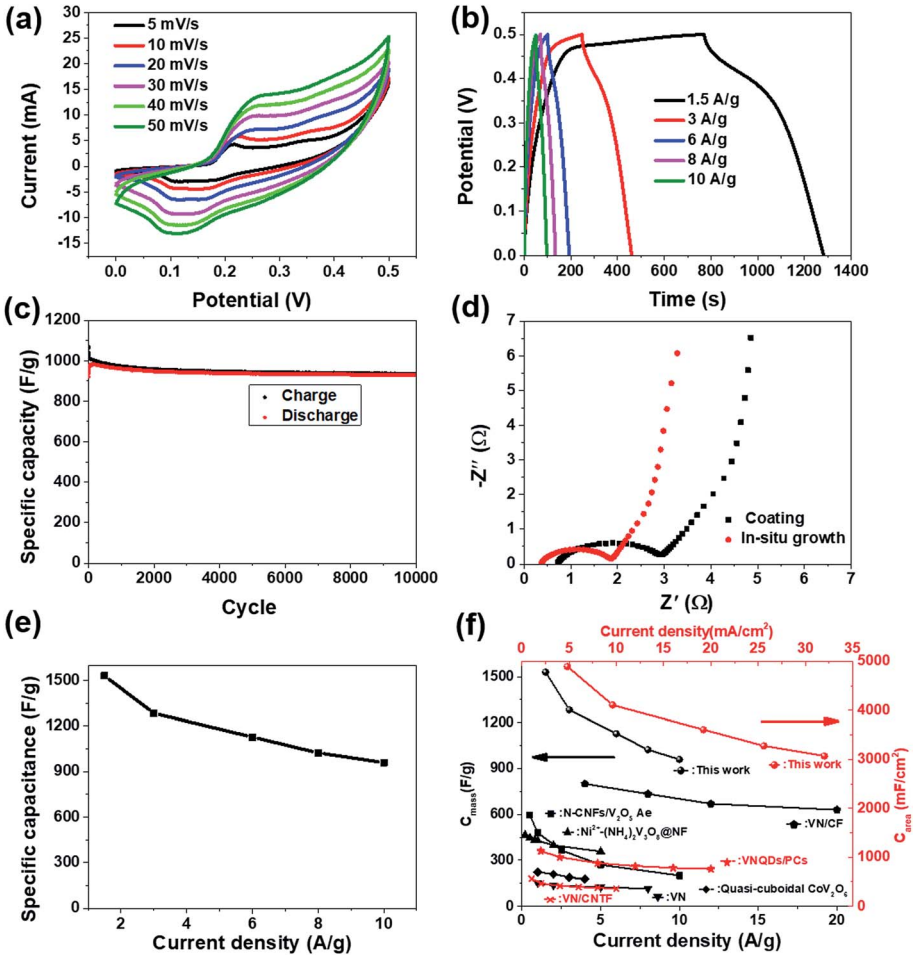

Fig. 4 (a) CV curves of the $(NH_4)_2V_{10}O_{25}\cdot 8H_2O$ urchin-like structure at various scan rates from 5–50 mV s^{-1}. (b) Galvanostatic charge–discharge curves at different current densities. (c) Cycling performance and (d) Nyquist plots of the $(NH_4)_2V_{10}O_{25}\cdot 8H_2O$ urchin-like structure. (e) Specific mass capacitances of the as-prepared $(NH_4)_2V_{10}O_{25}\cdot 8H_2O$ calculated according to (b) as a function of current density. (f) Comparison of C_{mass} and C_{area} of some reported vanadium based composites as active materials and the present work.[7,9,19–23]

semicircle diameter reflects the charge-transfer resistance (R_{ct}). Apparently, $(NH_4)_2V_{10}O_{25}\cdot 8H_2O$@Ni obtained through *in situ* growth possesses a much lower R_s and R_{ct} value compared with that of the material obtained by coating, which can be attributed to the binder-free effect of *in situ* growth. Moreover, the relatively steeper low-frequency tail of $(NH_4)_2V_{10}O_{25}\cdot 8H_2O$@Ni suggests greater electron diffusion. Therefore, all of these are beneficial for the electron storage properties of the $(NH_4)_2V_{10}O_{25}\cdot 8H_2O$@Ni electrode. The specific mass capacitance values were calculated as 1530, 1284, 1128, 1024 and 960 F g^{-1} at current density values of 1.5, 3, 6, 8 and 10 A g^{-1}, respectively. The corresponding areal capacitance and volumetric capacitance were also calculated and are shown in Fig. S4.† Clearly, both mass and areal capacitance values based on our $(NH_4)_2V_{10}O_{25}\cdot 8H_2O$ electrode exceed those of most reported vanadium-based materials (Fig. 4f).[7,9,19–23]

Finally, all-solid-state asymmetric supercapacitors (ASC) were assembled with $(NH_4)_2V_{10}O_{25}\cdot 8H_2O$@Ni foam as the positive electrode, RGO as the negative electrode and poly(vinyl alcohol) (PVA)–KOH gel as the electrolyte (Scheme 1). The mass ratio of active materials within the two opposite electrodes is based on the capacity balancing relation. As seen in Fig. 5a, with the voltage window of the RGO filling up −1.0 V to 0 V, the working potential of asymmetric supercapacitor devices hence is widened to 1.5 V. The CV curves with 0–1.5 V working window at various scan rates are shown in Fig. 5b and the well retained CV curves as the scan rate rises to 50 mV s^{-1} indicate the excellent rate capability. Based on the GCD results (Fig. 5c), the specific capacitances of the whole asymmetric supercapacitor were calculated to be 92.2, 88, 81.5, 75.6, 63.8 and 48.6 F g^{-1} at current densities of 0.4, 0.6, 1, 2, 4 and 8 A g^{-1}, respectively. As seen from the cycling performance as shown in Fig. 5d, the as-obtained asymmetric supercapacitor retains quite a stable capacitance through 5000 cycles and the slight increase in C_s could be ascribed to the enlargement of the electrochemical active volume of the two electrodes caused by the insertion and extraction of ions in the initial cycles.[28,29] The Ragone diagram plots the energy and power densities of the fabricated device, which were attained from calculations based on the galvanostatic discharge plots (Fig. 5e). The as-fabricated asymmetric

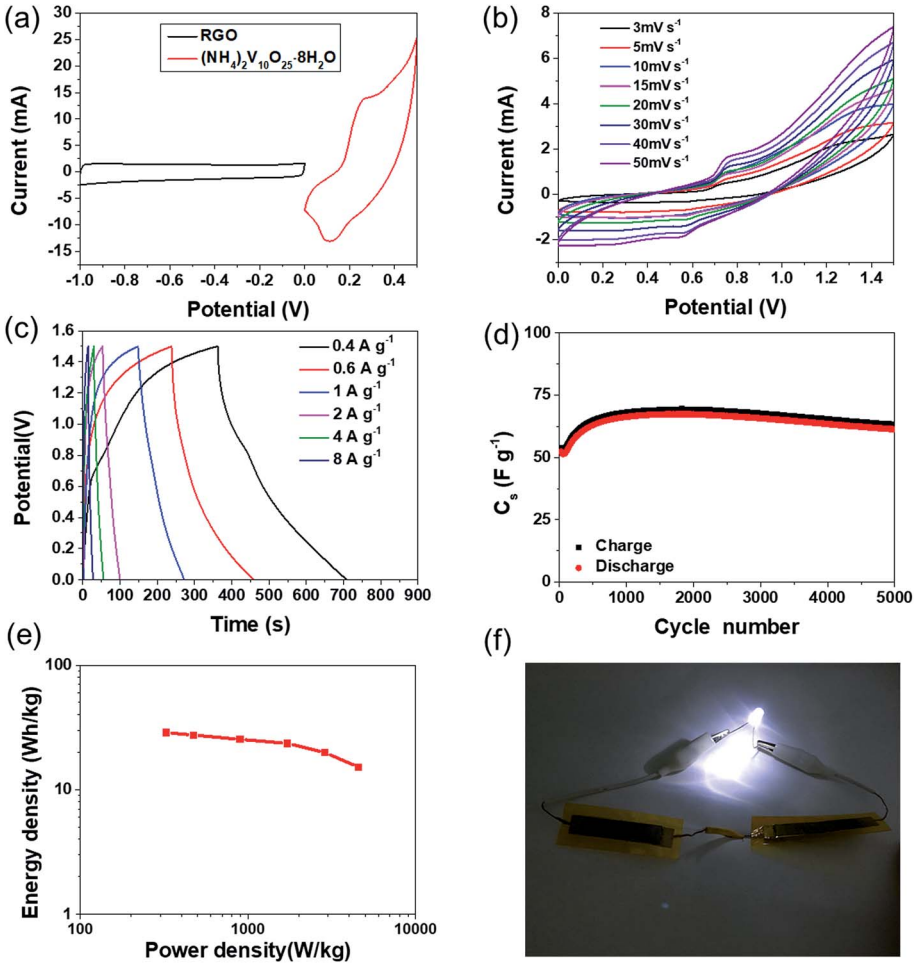

Fig. 5 (a) CV curves of the $(NH_4)_2V_{10}O_{25}\cdot 8H_2O$@Ni foam and RGO at a scan rate of 10 mV s^{-1}. (b) CV curves of the as-assembled asymmetric supercapacitor. (c) GCD curves of the as-assembled asymmetric supercapacitor. (d) Cycle performances of the as-assembled asymmetric supercapacitor. (e) Ragone plot of $(NH_4)_2V_{10}O_{25}\cdot 8H_2O$@Ni//PVA/KOH//RGO ASC. (f) Photograph of the LED indicator powered by two $(NH_4)_2V_{10}O_{25}\cdot 8H_2O$@Ni foam//PVA/KOH//RGO@Ni foam asymmetric supercapacitors connected in series.

supercapacitor exhibits an energy density of 28.8 W h kg^{-1} at a power density of 325 W kg^{-1}, and maintained 12 W h kg^{-1} at 4556.3 W kg^{-1}. Furthermore, two $(NH_4)_2V_{10}O_{25}\cdot 8H_2O$@Ni foam//PVA/KOH gel//RGO ASCs in series are able to light up one white LED indicator (Fig. 5f).

Conclusion

In summary, highly dispersed $(NH_4)_2V_{10}O_{25}\cdot 8H_2O$ urchin-like structures *in situ* decorated on highly conductive nickel foam have been successfully achieved using a novel one-step precipitation method. The composited $(NH_4)_2V_{10}O_{25}\cdot 8H_2O$@Ni electrode exhibited high C_{mass} (1530 F g^{-1} at 1.5 A g^{-1}) and C_{area} (4896 F cm^{-2} at 4.8 mA cm^{-2}), which exceed those of most previously reported vanadates and polyvanadates. The excellent energy storage performance should be attributed to the highly exposed active surface, the binder-free effect and the fast charge transfer at the $(NH_4)_2V_{10}O_{25}\cdot 8H_2O$@Ni interface. The $(NH_4)_2V_{10}O_{25}\cdot 8H_2O$@Ni//PVA/KOH//RGO device exhibits a comparable capacity of 92.2 F g^{-1} at a current density of 0.4 A g^{-1} and excellent cycling performance through 5000 cycles. Our study provides rational guidance toward the design of novel hierarchical nanostructures of vanadium-based compounds with superior electrochemical performances due to the significantly increased electrochemical active sites and shortened charge/ion diffusion.

Experimental

Fabrication of hybrid film-based electrodes

Typically, the hybrid electrode material was prepared using a simple one-step process as follows: nickel foam (5 cm × 1 cm × 0.15 mm, 110 ppi (pores per inch), 350 g m^{-2}) was successively pre-treated with acetone, absolute ethanol, deionized water, 2 M HCl solution and deionized water, each for 15–20 min, to ensure a clean surface. The cleaned nickel foam was then partially immersed in a 100 mL Teflon autoclave with a homogeneous solution of NH_4VO_3 (1.7 g) and H_2O (70 g), followed by heating the autoclave in an oven at 190 °C for 15 h to allow the growth of $(NH_4)_2V_{10}O_{25}\cdot 8H_2O$ urchin-like arrays on

the Ni foam. The nickel foam substrate, covered with $(NH_4)_2V_{10}O_{25}\cdot 8H_2O$ urchin-like hierarchical structures, was washed with H_2O and ethanol to remove surface ions and molecules using an ultrasonic bath cleaner, and then dried at 80 °C for 12 h to remove the adsorbed solvents. The mass of the nanowires on nickel foam was determined by subtracting the weight before deposition from the weight after deposition. The loading densities of the active materials were about 3.2 mg cm^{-2} for all electrodes.

Fabrication of RGO electrodes and asymmetric supercapacitors

Reduced graphene oxide (RGO) used in the experiment was purchased from Nanjing XF Nanomaterials and Technologies Co. Ltd. (diameter = 0.5–2 μm; thickness ~ 0.8 nm; monolayer ratio ~ 80%; purity ~ 99%). The RGO electrodes were fabricated using the method as follows: a mixture of RGO, 15 wt% of acetylene black (as an electrical conductor), 5 wt% of polytetrafluorene-ethylene (as a binder), and a small amount of ethanol was prepared by milling to produce a homogeneous paste. This paste was then pressed onto nickel foam current collectors to produce the RGO electrodes. To fabricate the asymmetric supercapacitor, the above two kinds of electrode were then pressed and combined with each other with PVA gel of KOH (3 M) as the solid electrolyte to assemble the full cell. The cell was encapsulated by flexible Kapton film with two pieces of copper wire connected to the edges of the two electrodes. The C_s of the asymmetric supercapacitor was calculated based on the total mass of both the negative and positive electrodes excluding the current collector.

Characterization

The morphologies were observed using scanning electron microscopy (SEM, S-4800, Hitachi). The SAED pattern and TEM images were obtained on a Philips CM200FEG field emission microscope. The crystalline structure was characterized by XRD patterns recorded in a Rigaku D/Max-kA diffractometer with Cu Kα radiation. X-ray photoelectron spectroscopy (XPS, PHI 5000C ESCA System) and energy dispersive X-ray spectroscopy (EDX, TSL, AMETEK) measurements were employed to investigate the elemental compositions of the samples.

Electrochemical measurement

The electrochemical properties of the as-obtained hybrid film-based electrodes were investigated using a three-electrode cell configuration at 25 °C. The nickel foam supported $(NH_4)_2V_{10}O_{25}\cdot 8H_2O$ urchin-like hierarchical structures acted directly as the working electrodes and were soaked in a 1 M KOH solution and degassed in a vacuum for 5 h before the electrochemical test. Platinum foil and a saturated calomel electrode (SCE) were used as the counter and reference electrodes, respectively. The cyclic voltammetry (CV), galvanostatic charge–discharge, and electrochemical impedance spectroscopy (EIS) measurements were conducted on a CHI 660B electrochemical workstation (Shanghai CH Instrument Company, China). The C_s of the hybrid film-electrode was calculated from galvanostatic charge–discharge curves as follows: $C_s = I \times \Delta t/(\Delta V \times m)$, where C_s (F g^{-1}) is the specific capacitance, I (A) is the discharge current, Δt (s) is the discharge time, ΔV (V) is the potential change during the discharge and m (g) is the mass of the active material in the electrode. The energy and power densities of the hybrid film-based electrodes were calculated as follows: $E = 0.5 \times C \times V^2$, $P_{ave} = E/\Delta t$, where E (W h kg^{-1}) is the energy density, V (V) is the cell voltage range. P_{ave} (W kg^{-1}) is the average power density and Δt (s) is the discharge time.

Conflicts of interest

There are no conflicts to declare.

Acknowledgements

This work was financially supported by the National Key Research and Development Program of China (2016YFB0100303), the National Natural Science Foundation of China (No. 51701042) and the Shanghai Rising-Star Program (16QA1400700).

References

1 (*a*) Y. Huang, M. Zhong, Y. Huang, M. S. Zhu, Z. X. Pei, Z. F. Wang, Q. Xue, X. M. Xie and C. Y. Zhi, *Nat. Commun.*, 2015, **6**, 8; (*b*) Y. Huang, M. S. Zhu, Y. Huang, Z. X. Pei, H. F. Li, Z. F. Wang, Q. Xue and C. Y. Zhi, *Adv. Mater.*, 2016, **28**, 8344.
2 (*a*) R. Ma, X. H. Liu, J. B. Liang, Y. Bando and T. Sasaki, *Adv. Mater.*, 2014, **26**, 4173; (*b*) P. Simon and Y. Gogotsi, *Nat. Mater.*, 2008, **7**, 845–854.
3 G. Q. Zhang and X. W. Lou, *Adv. Mater.*, 2013, **25**, 976–979.
4 L. Y. Yu, L. F. Hu, B. Anasori, Y. Y. Liu, Q. Z. Zhu, P. Zhang, Y. Gogotsi and B. Xu, *ACS Energy Lett.*, 2018, **3**, 1597–1603.
5 B. Xu, H. R. Wang, Q. Z. Zhu, N. Sun, B. Anasori, L. F. Hu, F. Wang, Y. B. Guan and Y. Gogotsi, *Energy Storage Materials*, 2018, **12**, 128–136.
6 D. Kundu, B. D. Adams, V. Duffort, S. H. Vajargah and L. F. Nazar, *Nat. Energy*, 2016, **1**, 16119.
7 D. Kundu, S. Vajargah, L. W. Wan, B. D. Adams, D. Prendergast and L. F. Nazar, *Energy Environ. Sci.*, 2018, **11**, 881–892.
8 G. F. Ren, R. B. Zhang and Z. Y. Fan, *Appl. Surf. Sci.*, 2018, **441**, 466–473.
9 T. Hu, Y. Y. Liu, Y. F. Zhang, Y. Nie, J. Q. Zheng, Q. S. Wang, H. M. Jiang and C. G. Meng, *Microporous Mesoporous Mater.*, 2018, **262**, 199–206.
10 W. G. Sun, H. Gao, K. Zhang, Y. D. Liu and G. M. Wu, *Carbon*, 2018, **132**, 667–677.
11 H. Wang, H. Yi, X. Chen and X. Wang, *J. Mater. Chem. A*, 2014, **2**, 1165–1173.
12 Q. F. Zhou, Y. Gong and J. H. Lin, *Appl. Surf. Sci.*, 2018, **439**, 33–44.
13 Y. Wang, K. Takahashi, K. Lee and G. Z. Cao, *Adv. Funct. Mater.*, 2006, **16**, 1133–1144.

14 A. S. Arico, P. Bruce, B. Scrosati, J. M. Tarascon and W. Van Schalkwijk, *Nat. Mater.*, 2005, **4**, 366–377.
15 A. M. Cao, J. S. Hu, H. P. Liang and L. J. Wan, *Angew. Chem., Int. Ed.*, 2005, **44**, 4391–4395.
16 J. K. Lee, G. P. Kim, I. K. Song and S. H. Baeck, *Electrochem. Commun.*, 2009, **11**, 1571–1574.
17 H. Y. Wang, K. L. Huang, S. Q. Liu, C. H. Huang, W. J. Wang and Y. Ren, *J. Power Sources*, 2011, **196**, 788–792.
18 J. Elias, C. L. Clement and M. Bechelany, *Adv. Mater.*, 2010, **22**, 1607–1612.
19 B. Wang, H. B. Wu, L. Yu, R. Xu, T. T. Lim and X. W. Lou, *Adv. Mater.*, 2012, **24**, 1111–1116.
20 Q. M. Gan, H. N. He, K. M. Zhao, Z. He, S. Q. Liu and S. P. Yang, *ACS Appl. Mater. Interfaces*, 2018, **10**, 7031–7042.
21 H. W. Gao, X. H. Wang, G. H. Wang, C. Hao, S. S. Zhou and C. X. Huang, *Nanoscale*, 2018, **10**, 10190–10202.
22 J. B. Guo, Q. Q. Zhang, J. Sun, C. W. Li, J. X. Zhao, Z. Y. Zhou, B. He, X. N. Wang, P. Man, Q. L. Li, J. Zhang, L. Y. Xie, M. X. Lia and Y. G. Yao, *J. Power Sources*, 2018, **382**, 122–127.
23 Z. Q. Hou, K. Guo, H. Q. Li and T. Y. Zhai, *CrystEngComm*, 2016, **18**, 3040–3047.
24 Y. C. Wang, H. Chai, H. Dong, J. Y. Xu, D. Z. Jia and W. Y. Zhou, *ACS Appl. Mater. Interfaces*, 2016, **8**, 27291–27297.
25 Y. L. Yang, L. Zhao, K. W. Shen, Y. Liu, X. N. Zhao, Y. G. Wu, Y. Q. Wang and F. Ran, *J. Power Sources*, 2016, **333**, 61–71.
26 G. H. An, D. Y. Lee and H. J. Ahn, *J. Mater. Chem. A*, 2017, **5**, 19714–19720.
27 R. D. Smith, M. S. Prévot, R. D. Fagan, S. Trudel and C. P. Berlinguette, *J. Am. Chem. Soc.*, 2013, **135**, 11580–11586.
28 M. Yu, W. C. Li, G. H. He, L. Zhang and M. Li, *J. Mater. Chem. A*, 2015, **3**, 20619–20626.
29 D. Rangappa, K. D. Murukanahally, T. Tomai, A. Unemoto and I. Honma, *Nano Lett.*, 2012, **12**, 1146–1151.